Solder-free Electrical Joule Welding of Macroscopic Graphene Assemblies

Yingjun Liu [a,e], Chunyuan Liang [b,e], Anran Wei [c,e], Yanqiu Jiang [a], Qishi Tian [a], Ying Wu [a], Zhen Xu [a,], Yinfeng Li [c,*], Fan Guo [a], Qiuyan Yang [a], Weiwei Gao [a], Hongtao Wang [d,*], Chao Gao [a,*]*

[a] MOE Key Laboratory of Macromolecular Synthesis and Functionalization, Department of Polymer Science and Engineering, Key Laboratory of Adsorption and Separation Materials & Technologies of Zhejiang Province, Zhejiang University, 38 Zheda Road, Hangzhou 310027, P. R. China.

[b] School of Materials Science and Engineering, Zhejiang University, 38 Zheda Road, Hangzhou 310027, P. R. China.

[c] Department of Engineering Mechanics, School of Naval Architecture, Ocean and Civil Engineering, State Key Laboratory of Ocean Engineering, Shanghai Jiao Tong University, Collaborative Innovation Center for Advanced Ship and Deep-Sea Exploration, Shanghai 200240, P. R. China.

[d] Center for X-Mechanics, Zhejiang University, 38 Zheda Road, Hangzhou 310027, P. R. China.

[e] These authors contributed equally to this work.

* Corresponding author

E-mail addresses: zhenxu@zju.edu.cn (Z. Xu), liyinfeng@sjtu.edu.cn (Y. Li), htw@zju.edu.cn (H. Wang), chaogao@zju.edu.cn (C. Gao).

Keywords: Graphene assemblies, Joule heating, Welding, *In-situ* TEM, Molecular dynamics.

Abstract: Welding is an important convenient methodology to realize robust coalescence of individual metallic or polymeric objects through local melting of contact boundaries. However, how to firmly conjoin the refractory graphene-based materials via conventional welding remains an open question because of their non-melting nature. In this work, we report an efficient solder-free approach to weld individual macroscopic graphene assemblies via electrical Joule heating. Graphene-based materials with different architectures, including graphene fibers, films and foams, are covalently welded together with high joint strength. The welding mechanism was studied by in-situ TEM and molecular dynamic simulations. We attributed the unique welding behavior to the defect-facilitated cross-linking between graphene layers at contact interface. The facile electrical Joule welding strategy provides a new reliable connection method for carbon materials, enabling the direct assembling of macroscopic graphene materials to sophisticated 3D configurations.

1. Introduction

Welding is a reliable connection methodology in modern manufacturing processes, which firmly connects two or more workpieces of the same or dissimilar constitutions to achieve complete interfacial coalescence [1-4]. The most practical welding technique is the fusion welding for metallic and thermoplastic polymeric components, which is achieved by the melting and merging of local contact fronts. As graphene materials become increasingly promising in practical applications, a significant issue is intuitively emerging: how to firmly connect graphene assemblies, just as welding of conventional metallic and polymeric materials. Generally, macroscopically assembled graphene materials possess combined merits of excellent mechanical and electrical/thermal properties, but these exceptional performances will

be degraded severely by the poor interfacial connections among different components in complex architectures [5-9], as in the cases of carbon materials such as fabrics of carbon fibers and carbon nanotube (CNT) fibers [10]. This emerged connection issue needs to be solved but remains greatly challenging. In contrast to metallic and polymeric materials, graphene is non-fusible below its decomposition temperature because of the strong C-C bonding, making conventional welding methods inapplicable. It is highly desirable to explore a novel and efficient connection method for graphene assemblies to fabricate integrations without degrading their overall performances.

Several physical or chemical approaches have been proposed for the welding of carbon materials. The deposition of amorphous carbon layers was used to physically connect crossing multiwalled CNTs, broken CNTs, and macroscopic CNT fibers [11-13]. A covalent welding of crossing single-walled CNTs was observed in the microscopic scale under strong electron beam radiation [14]. Hu and co-workers constructed a three-dimensional (3D) interconnected network using carbon nanofibers by constructing graphitic nodes between adjacent nanofibers [10, 15]. As for graphene-based materials, irradiation and organic cross-linking agent have been used to realize sheet-sheet welding [16-18]. Additionally, the moisture and water induced fusion method was applied to connect graphene oxide (GO) assemblies by hydrogen-bonding interactions [5, 19, 20]. This method only works for hydrophilic GO components. Therefore, to realize the direct connection of macroscopic graphene materials by effective covalent welding still remains in suspension.

Here, we report an efficient solder-free electrical Joule welding method to tightly conjoin macroscopic graphene assemblies. Graphene-based architectures with different dimensions,

such as graphene fibers, films and foams, can be firmly bonded together after electrical Joule heating treatment while maintaining their structural integrity and conductivity. This Joule welding strategy not only enables strong coalescence of multidimensional macroscopic graphene materials, but also provides a new pathway for the bottom-up manufacture of sophisticated 3D architectures from all-solid-state carbon-based constituents.

2. Results and discussion

Figure 1a schematically shows the experimental set-up for the welding of graphene films (GFs) that chemically reduced by HI (GF-HI). The GF-HIs were clamped by highly pure graphite electrodes on a quartz substrate and were stacked in a straight line in a vacuumed chamber (5×10^{-5} mbar, Figure S1 in the Supporting Information). A voltage was applied on the graphite electrodes, causing a temperature rise due to the Joule heating effect. Bright visible light emitted from the Joule heated GF-HI strips (width W=2 mm, length L=10, 20 mm) with different patterns, as shown in Figure 1b. After cooling to room temperature, the stripes were welded into freestanding integrated pieces (Figure 1c) because of strong inter-stripe connections. No clear interface between the welded films was observed from cross-sections by scanning electron microscopy (SEM) (Figure 1d), indicating that contact parts were bonded closely, and the interfacial inhomogeneity was eliminated.

We measured the temperature and electrical conductivity responses during the welding process by a programmed increase of the voltage from 5 to 20 V at an interval of 5 V (Figure 2a). The voltage was increased stepwise and kept for 30 min at each stage to avoid damages induced by rapid thermal shock. The temperature of the film (width W=2 mm, length L=10 mm) was recorded on-line by two commercial noncontact two-color pyrometers (Fluke Endurances

series E2RL-F1-L-0-0 for 250~1200 °C and Raytek Marathon MR1SC for 1000~3000 °C). The sample temperature increased with the applied voltage due to increased current density [21-25]. The film began to emit visible light once the voltage surpassed a threshold value of ~10 V, and its brightness increased with the applied voltage as shown by a series of snapshots taken during the welding process (Figure 2a).

We tracked the interface contact resistance as a function of Joule heating time using a four-probe method (Figure S2). In this testing configuration, the intrinsic resistance change of films was excluded. After the programed welding, the contact resistance shows a monotonically decreasing profile by two orders of magnitude from 22.6 to 0.28 Ω (Figure 2b). Therefore, the decreased contact resistance could be attributed to the structural change of the contact interface during the Joule heating process, which will be discussed later. As a comparison, we measured electrical conductivity of mechanically stacked films without welding, which were joule heated in vacuum at the same temperature. According to *I-V* curves, the electrical conductivity of the welded film was 4.67 times higher than that of the mechanically stacked films (Figure 2c). The LED lamp connected by the welded films showed higher brightness than that connected by the mechanically stacked films (Figure 2c, inset), further demonstrating the improved interlayer electrical conductivity by Joule welding. The decreased contact resistance and the increased electrical conductivity suggest that the coalescence may form at the overlapped part of the welded films and contribute to the electron transport through the film interface.

The structural evolution of GF-HI was characterized by X-ray photoelectron spectroscopy (XPS), Raman spectroscopy, and X-ray diffraction (XRD). The C/O atomic ratio (Figure 2d)

of GF-HI after Joule heating increases from 6.4 to 21.3. High-solution C 1s spectrum of GF-HI (Figure S3) can be deconvoluted into four peaks, corresponding to C–C/C=C (284.6 eV), C–O (286.6 eV), C=O (287.8 eV), and O–C=O (289.0 eV) [26]. Peaks of oxygen-containing groups almost disappeared after the welding process, confirming the mostly removed oxygenated moieties [27-29]. In Raman spectra, the intensity ratio (I_D/I_G) of the D (at ~1350 cm^{-1}, related to the defect-induced Raman process) to G peak at ~1585 cm^{-1} dramatically decreased from 1.10 to 0.08 after welding (Figure 2e), implying an effective recovery of structural defects by Joule heating, as previously reported [30, 31]. In addition, a prominent 2D band at 2720 cm^{-1} was observed for the welded film. The XRD pattern (Figure 2f) of initial GF-HI shows a (002) reflection peak at 24.16° with a full width at half maximum (FWHM) of 2.12°. While for the welded film, the characteristic peak shifts to 25.98° and becomes much narrower with a FWHM of 1.13°. The calculated interspace distance reduces from 0.36 nm for the GF-HI to 0.34 nm for the welded film, which is consistent with the decline of oxygen containing groups as illustrated in XPS spectra.

Lap shear testing is widely used to evaluate the adhesive strength between joined interfaces [32, 33]. Generally, there are two typical breakage behaviors during the lap shear testing – breaking at the adhesion interface and at the bulk part (Figure 3a). Figure 3b shows the shear stress-strain curves of Joule heated films with an overlapping area of 4 mm^2. The welded GF-HI exhibits a breakage strength up to 72 KPa and a failure strain of 6.9%. The film broke at the bulk part rather than at the overlapped section (Figure 3a, right second). Thus, we infer that the contact interface is coalesced tightly after Joule heating treatment and some interlayer bonds should form to provide enough cohesive force. Furthermore, we welded other

three kinds of GFs that were pre-annealed at 1000 °C, 2000 °C and 2800 °C in graphitization furnace, signed as GF-1000, GF-2000 and GF-2800, respectively. Tensile failures of all welded pre-annealed films occurred at the overlapped section (Figure 3a, right first), resulting in joint strengths of 20.78 KPa, 14.96 KPa, 11.41 KPa, respectively (Figure 3b). Since the content of oxygen-containing functional groups in GF decreases with pre-annealing temperature, it is interesting to note that the gradually reduced joint strength is in line with the decreasing content of oxygen-containing groups. Therefore, we infer that the oxygen-containing functional groups (structural defects) play important roles in the heat-welding process and the welding strength.

To reveal the tensile-failure mechanism of welded GF-HI films, the morphology of the fracture interface was examined by SEM. We tore the welded section of GF-HI for analysis. The torn interface is rather rough and riddled with numerous fragments (Figure 3a and S4), strikingly different from the smooth morphology of the upper surface (Figure S5). Meanwhile, some graphene flakes are observed to be peeled off and stand vertically on the torn surface, which is in accordance with typical adhesive failure model (Figure S6) [34]. Generally, there are three possible primary interlayer interactions between chemically converted graphene sheets: hydrogen bonding, covalent bonding and π-π stacking interactions [35, 36]. For the welded GF-HI obtained by Joule heating with a temperature up to 2000 °C, no hydrogen bonding interaction exists because most of the oxygen-containing groups are eliminated (Figure 2a and S3). Thus, covalent bonds formed at the contact interface or π-π interactions may account for the welding phenomenon. The failure morphology for the welded GF-1000 is similar to that of GF-HI, while the degree of joint destruction weakens obviously (Figure 3d). For GF-2000, most of the interface is flat with only a few of graphene flakes tearing off the

matrix (Figure 3e). The whole failure interface is smooth and intact without any fracture debris for GF-3000 (Figure 3f), which is almost the same as the surface morphology before welding (Figure S7). Most of the oxygen-containing groups are removed and the structural defects are repaired in films pre-annealed at high temperatures (Figure S8), making π-π interaction the primary adhesive force at the contact interface. Therefore, we can conclude that the weak π-π interaction should be responsible for the relatively low joint strengths of welded pre-annealed films, while the strong bonded interface accounts for the robust welding behavior of GF-HI.

To study the electrical connection of graphene sheets at the micro-scale level, we tried to conjoin separated reduced GO (rGO) sheets by *in-situ* transmission electron microscope (TEM) equipped with a micro-electro-mechanical system (Figure S9). With a constant voltage applied on two separated rGO sheets, current is generated suddenly once they overlap together. Sequential TEM images and corresponding schematic illustrations show the "approaching-welding-stretching" process (Figure 4). Similar to the welding of macroscopic films, it is observed that the Joule welding strength is highly dependent on the applied voltage in this micro system. When the voltage was lower than 3 V (Figure S10a), the interfacial connection was too weak to robustly bond the sheets together, as demonstrated by the unchanged morphology after stretching apart (Figure 4a, b, Video S1). When the bias voltage reached 4 V (Figure S10b), the current increased gradually after the overlapping of two sheets, suggesting the merging of rGO sheets (Figure 4d, the third one), which is consistent with previous report [37]. Consequently, the overlap region was tightly bonded and one rGO sheet was torn into two parts under tensile stress (Figure 4c, d, and Video S2). This breakage behavior only happens when the interfacial adhesion after welding is strong enough to allow the tearing of

graphene sheet but not the sliding between them (Figure 4a, b). Additionally, another set of experiment also confirmed the welding of rGO sheets (Figure S11, Video S3). The Joule welding at the micro-scale level agrees well with the macroscopic lap shear testing.

To understand the mechanism of the welding behavior at atomic scale, molecular dynamic (MD) simulations were conducted. Bilayer graphene sheets with vacancy defects were used as a model of contact surface to simulate the welding process. The snapshots of the bilayer structure evolution taken at three representative temperatures are shown in Figure 5a-c. Interlayer covalent bonds began to form at ~1200 °C and the number of the interlayer bonding increased with the increasing temperature. The bilayer graphene welded at 2000 ℃ possessed higher normal tensile strength than graphene welded at 1600 and 1200 ℃ (Figure S12). This is attributed to the enhanced reactivity of carbon atoms at defective sites and the increased dangling bonds formed at defects, which contribute to increase the tensile strengths of the welded structures by interlayer covalent cross-linking (Figure S13).

From the top view of the crossover region (Figure 5d, e), the bridging bonds between bilayer graphene sheets mainly form around defective sites. We further studied the influence of vacancy density on the welding behavior. The number of interlayer bonding increases with the initial defect density (Figure 5f-h). The stress-displacement curves of welded bilayer graphene with different defect densities are shown in Figure 5i, where the peak value represents the ultimate strength. It is obvious that the bilayer graphene with higher defect density possesses higher joint strength. Therefore, we can conclude that the denser structural defects in GF-HI facilitate the formation of seamless junctions at the overlapped part under Joule

heating, while lower defect densities of preannealed GFs result in fewer interlayer bonds and weaker joint strengths. The simulation results also agree well with the experimental phenomena.

This facile welding approach enables the fabrication of complex 3D architectures from 2D tailor-cut sheets. A graphene ring (Figure 6a) and Möbius band (Figure 6b) were prepared by welding two ends of a GF-HI strip. Figure 6c shows a "K" shaped structure with a welding point at the center of two individual films. A more sophisticated stretchable kirigami architecture (Figure 6d) were constructed using the basic "K" shaped constituents. The Joule welding method is also feasible to the coalescence of different dimensional graphene-based assemblies. As shown in Figure 6e, three pieces of graphene films are bridged by three graphene fibers. Additionally, two individual rectangular chemically reduced foams with sizes of 2.0 cm × 2.0 cm × 1.0 cm were also welded into a freestanding monolithic structure with high integrity (Figure 6f). Welding permits tremendous freedom in structure design. All these complex free-standing architectures highlight the versatility of this welding approach, which will certainly broaden the application scope of the high temperature manufacturing technique. Furthermore, in the emerging all-carbon electronics, this unique Joule welding technique helps to eliminate the contact resistance or Schottky barrier caused by traditional heterogeneous contacts.

3. Conclusion

We report an efficient solder-free electrical Joule heating method to weld the separated graphene assemblies. The welded graphene film shows strong joint strength and significantly enhanced electrical conductivity while maintaining their structural integrity. The robust welding behavior is attributed to the bridging bonds formed at the interface of two graphene

films with structural defects, as supported by *in-situ* TEM and MD simulations. This simple yet effective welding technique opens the avenue to direct construct carbon-assemblies into well-designed architectures.

4. Experimental section:

4.1 Preparation of assemblies

Aqueous GO solutions (5 mg/mL) were purchased from Hangzhou Gaoxi Technology Co. Ltd. (www.gaoxitech.com). The graphene assemblies, including graphene films, fibers, and foams, were prepared according to the literature [38-40]. Typically, GO films, fibers, foams were prepared by bar-coating, wet-spinning, and freeze-drying method, respectively, followed by chemical reduction using HI.

4.2 Electrical Joule Welding Process

Electrical Joule heating was conducted in a vacuum chamber at a pressure of 5×10^{-5} mbar. Graphene assemblies were clamped by highly pure graphite blocks and suspended on a quartz substrate. An auto range DC power supply (ITECH IT6522D) was used to provide bias voltage on graphite electrodes to achieve the Joule welding. The temperature of samples during the welding process was recorded continuously by two commercial two-color pyrometers (Raytek Marathon MR1SC for 1000~3000 °C and Fluke Endurances series E2RL-F1-L-0-0 for 250~1200 °C).

4.3 In-situ TEM observations

In-situ TEM were performed on a JEOL JEM-2100 microscope at 200 kV. Dilute GO aqueous suspensions were dropped on two micro electrodes with nanotips, followed by reduction using HI vapor at 90 ℃ for 1 h. In-situ “approaching-welding-stretching” at the

micro-scale level was controlled by a home-made TEM holder with electric biasing and nanomanipulation functions. A Keithley source meter 2460 was used to supply constant voltages on rGO sheets and measure the current across the samples.

4.4 Characterization techniques

Morphologies of the samples were observed on a Hitachi S4800 field-emission SEM at 10 kV. Raman measurement was performed by a Renishaw inVia-Reflex Raman microscope at an excitation wavelength of 532 nm. XRD patterns were recorded on an X'Pert PRO diffractometer (PANalytical) using Cu Kα1 radiation with an X-ray wavelength of 0.154 nm. XPS measurement was carried out on an ESCALAB 250 photoelectron spectrometer (ThermoFisher Scientific) with Al Kα as X-ray source. Contact resistances of the welded interface were measured by a four-probe method using Keithley 2460 source meter. Mechanical performances were evaluated on the Instron universal testing machine (Instron 2344) with a gauge length of 10 mm and a loading rate of 1.0 mm/min.

4.5 MD simulations

The simulations were carried out using Large-scale Atomic/Molecular Massively Parallel Simulator (LAMMPS) package [41]. Interactions between carbon atoms were described by the Adaptive Intermolecular Reactive Empirical Bond Order potential (AIREBO) [42] which has been widely used for studying the thermal and mechanical properties of carbon-based nanomaterials [43-45]. All the bilayer graphene models used in simulations have the same size of 10 nm × 4 nm, with single vacancy defects randomly distributed in graphene layers. Periodic boundary condition was applied along the in-plane direction, while the out-of-plane direction was confined to eliminate excessive vibrations of the atoms under Joule heating. The time step

was set as 0.01 fs. All the atom models were fully relaxed by energy minimization at room temperature (300 K) for 50000 time steps before welding to achieve equilibrium. Then the equilibrium structures were heated to 3000 K in 400000 time steps under NVT ensemble controlled by the Nosé−Hoover thermostat. The welded bilayer graphene was obtained after the heating process. In order to evaluate the effect of welding, uniaxial tension and interlayer shear were applied to the welded bilayer graphene. The welded structure was stretched at a strain rate of 0.01%/ps by scaling all atomic coordinates for the uniaxial tension, with each stretching step followed by a relaxation of 100 steps. The stretching and relaxation routine were repeated until complete failure of the welded bilayer graphene. For the interlayer shear, the bottom graphene layer after welding was fixed by specifying the velocity and the force of atoms equal to zero, while the upper graphene layer was moved. The atomic stress of individual atoms in the upper graphene layer was calculated according to equation [46, 47]

$$\sigma^{\alpha}{}_{ij} = \frac{1}{\Omega^{\alpha}}\left(\frac{1}{2} m^{\alpha} v_i^{\alpha} v_j{}^{\alpha} + \sum_{\beta=1,n} r_{\alpha\beta}{}^{j} f_{\alpha\beta}{}^{i}\right) \qquad (1)$$

where i and j denote indices in Cartesian systems; α and β are the atomic indices; m^{α} and v^{α} denote the mass and velocity of atom α, respectively; $r_{\alpha\beta}$ is the distance between atoms α and β; Ω^{α} is the atomic volume of atom α. The stress of the upper graphene layer is obtained by averaging stresses of all the atoms in the layer. The thickness of graphene layer is assumed to be 0.34 nm as suggested in a previous study [48].

Note

The authors declare no competing financial interest.

Acknowledgments

This work is supported by the National Natural Science Foundation of China (Nos. 51533008, 21325417, 21622407, 51603183, 11402145, 11725210), National Key R&D Program of China (No. 2016YFA0200200), Fundamental Research Funds for the Central Universities (Nos. 2017QNA4036, 2017XZZX008-06), Hundred Talents Program of Zhejiang University (188020*194231701/113), the Open Fund of State Key Laboratory of IPOC, the China Postdoctoral Science Foundation (Nos. 2017M620241, 2017M621927), and the National Postdoctoral Program for Innovative Talents (No. BX201700209). The computational support for this work was provided by Center for HPC, Shanghai Jiao Tong University.

Appendix A. Supplementary data

Supplementary data related to this article can be found at https://doi.org/10.1016/j.mtnano.2018

References

[1] G. Çam, M. Koçak, Progress in joining of advanced materials, Int. Mater. Rev. 43 (1998) 1-44.

[2] S. Kou, Welding metallurgy, John Wiley & Sons 2003.

[3] F. Balle, G. Wagner, D. Eifler, Ultrasonic metal welding of aluminium sheets to carbon fibre reinforced thermoplastic composites, Adv. Eng. Mater. 11 (2009) 35-39.

[4] H. Jafarlou, K. Hassannezhad, H. Asgharzadeh, G. Marami, Enhancement of mechanical properties of low carbon steel joints via graphene addition, Mater. Sci. Technol. 34 (2018) 455-467.

[5] Z. Li, Z. Xu, Y. Liu, R. Wang, C. Gao, Multifunctional non-woven fabrics of interfused graphene fibres, Nat. Commun. 7 (2016) 13684.

[6] H. Cheng, Y. Huang, G. Shi, L. Jiang, L. Qu, Graphene-based functional architectures: sheets regulation and macrostructure construction toward actuators and power generators, Acc. Chem. Res. 50 (2017) 1663-1671.

[7] Z. Li, Z. Liu, H. Sun, C. Gao, Superstructured assembly of nanocarbons: fullerenes, nanotubes, and graphene, Chem. Rev. 115 (2015) 7046-7117.

[8] K.H. Kim, Y. Oh, M. Islam, Graphene coating makes carbon nanotube aerogels superelastic and resistant to fatigue, Nat. Nanotech. 7 (2012) 562.

[9] Z. Chen, W. Ren, L. Gao, B. Liu, S. Pei, H.-M. Cheng, Three-dimensional flexible and conductive interconnected graphene networks grown by chemical vapour deposition, Nat. Mater. 10 (2011) 424.

[10] Y. Yao, K.K. Fu, S. Zhu, J. Dai, Y. Wang, G. Pastel, Y. Chen, T. Li, C. Wang, T. Li, L. Hu, Carbon welding by ultrafast joule heating, Nano Lett. 16 (2016) 7282-7289.

[11] M. Wang, J. Wang, Q. Chen, L.M. Peng, Fabrication and electrical and mechanical properties of carbon nanotube interconnections, Adv. Funct. Mater. 15 (2005) 1825-1831.

[12] D. Wei, Y. Liu, The intramolecular junctions of carbon nanotubes, Adv. Mater. 20 (2008) 2815-2841.

[13] Z. Lin, X. Gui, Q. Gan, W. Chen, X. Cheng, M. Liu, Y. Zhu, Y. Yang, A. Cao, Z. Tang, In-Situ Welding carbon nanotubes into a porous solid with super-high compressive strength and fatigue resistance, Sci. Rep. 5 (2015) 11336.

[14] M. Terrones, F. Banhart, N. Grobert, J.-C. Charlier, H. Terrones, P. Ajayan, Molecular junctions by joining single-walled carbon nanotubes, Phys. Rev. Lett. 89 (2002) 075505.

[15] Y. Yao, Z. Huang, P. Xie, S.D. Lacey, R.J. Jacob, H. Xie, F. Chen, A. Nie, T. Pu, M.

Rehwoldt, D. Yu, M.R. Zachariah, C. Wang, R. Shahbazian-Yassar, J. Li, L. Hu, Carbothermal shock synthesis of high-entropy-alloy nanoparticles, Science 359 (2018) 1489-1494.

[16] H. Li, S. Dai, J. Miao, X. Wu, N. Chandrasekharan, H. Qiu, J. Yang, Enhanced thermal conductivity of graphene/polyimide hybrid film via a novel “molecular welding” strategy, Carbon 126 (2018) 319-327.

[17] H. Wang, N. Li, Z. Xu, X. Tian, W. Mai, J. Li, C. Chen, L. Chen, H. Fu, X. Zhang, Enhanced sheet-sheet welding and interfacial wettability of 3D graphene networks as radiation protection in gamma-irradiated epoxy composites, Compos. Sci. Technol. 157 (2018) 57-66.

[18] T. Zhu, K. Teng, J. Shi, L. Chen, Z. Xu, A facile assembly of 3D robust double network graphene/polyacrylamide architectures via γ-ray irradiation, Compos. Sci. Technol. 123 (2016) 276-285.

[19] H. Cheng, Y. Huang, Q. Cheng, G. Shi, L. Jiang, L. Qu, Self-Healing Graphene Oxide Based Functional Architectures Triggered by Moisture, Adv. Funct. Mater. 27 (2017) 1703096.

[20] C. Luo, C.N. Yeh, J.M.L. Baltazar, C.L. Tsai, J. Huang, A Cut-and-Paste Approach to 3D Graphene-Oxide-Based Architectures, Adv. Mater. 30 (2018) 1706229.

[21] D. Yu, L. Dai, Voltage-induced incandescent light emission from large-area graphene films, Appl. Phys. Lett. 96 (2010) 143107.

[22] M. Freitag, H.-Y. Chiu, M. Steiner, V. Perebeinos, P. Avouris, Thermal infrared emission from biased graphene, Nat. Nanotech. 5 (2010) 497.

[23] Y. Chen, Y. Li, Y. Wang, K. Fu, V.A. Danner, J. Dai, S.D. Lacey, Y. Yao, L. Hu, Rapid, in situ synthesis of high capacity battery anodes through high temperature radiation-based thermal

shock, Nano Lett. 16 (2016) 5553-5558.

[24] Y. Yao, K.K. Fu, C. Yan, J. Dai, Y. Chen, Y. Wang, B. Zhang, E. Hitz, L. Hu, Three-dimensional printable high-temperature and high-rate heaters, ACS Nano 10 (2016) 5272-5279.

[25] Y.D. Kim, H. Kim, Y. Cho, J.H. Ryoo, C.-H. Park, P. Kim, Y.S. Kim, S. Lee, Y. Li, S.-N. Park, Y.S. Yoo, D. Yoon, V.E. Dorgan, E. Pop, T.F. Heinz, J. Hone, S.-H. Chun, H. Cheong, S.W. Lee, M.-H. Bae, Y.D. Park, Bright visible light emission from graphene, Nat. Nanotech. 10 (2015) 676.

[26] J. Chen, B. Yao, C. Li, G. Shi, An improved Hummers method for eco-friendly synthesis of graphene oxide, Carbon 64 (2013) 225-229.

[27] Z. Xu, Y. Liu, X. Zhao, L. Peng, H. Sun, Y. Xu, X. Ren, C. Jin, P. Xu, M. Wang, C. Gao, Ultrastiff and Strong Graphene Fibers via Full-Scale Synergetic Defect Engineering, Adv. Mater. 28 (2016) 6449-6456.

[28] G. Xin, T. Yao, H. Sun, S.M. Scott, D. Shao, G. Wang, J. Lian, Highly thermally conductive and mechanically strong graphene fibers, Science 349 (2015) 1083-1087.

[29] Y. Wang, Y. Chen, S.D. Lacey, L. Xu, H. Xie, T. Li, V.A. Danner, L. Hu, Reduced graphene oxide film with record-high conductivity and mobility, Mater. Today 21 (2017) 186-192.

[30] Y. Chen, K. Fu, S. Zhu, W. Luo, Y. Wang, Y. Li, E. Hitz, Y. Yao, J. Dai, J. Wan, V.A. Danner, T. Li, L. Hu, Reduced graphene oxide films with ultrahigh conductivity as Li-ion battery current collectors, Nano Lett. 16 (2016) 3616-3623.

[31] W. Bao, A.D. Pickel, Q. Zhang, Y. Chen, Y. Yao, J. Wan, K.K. Fu, Y. Wang, J. Dai, H. Zhu, D. Drew, M. Fuhrer, C. Dames, L. Hu, Flexible, high temperature, planar lighting with large scale printable nanocarbon paper, Adv. Mater. 28 (2016) 4684-4691.

[32] D. Kline, R. Wool, Polymer welding relations investigated by a lap shear joint method, Polym. Eng. Sci. 28 (1988) 52-57.

[33] Y.-L. Shen, N. Chawla, E. Ege, X. Deng, Deformation analysis of lap-shear testing of solder joints, Acta Mater. 53 (2005) 2633-2642.

[34] G. Jorgensen, K. Terwilliger, J. DelCueto, S. Glick, M. Kempe, J. Pankow, F. Pern, T. McMahon, Moisture transport, adhesion, and corrosion protection of PV module packaging materials, Sol. Energy Mater. Sol. Cells 90 (2006) 2739-2775.

[35] D. Li, M.B. Müller, S. Gilje, R.B. Kaner, G.G. Wallace, Processable aqueous dispersions of graphene nanosheets, Nat. Nanotech. 3 (2008) 101.

[36] Z. Xu, H. Sun, X. Zhao, C. Gao, Ultrastrong fibers assembled from giant graphene oxide sheets, Adv. Mater. 25 (2013) 188-193.

[37] B. A., B.r. F., M.H. Rümmeli, B. Büchner, L.M.K. Vandersypen, Graphene at High Bias: Cracking, Layer by Layer Sublimation, and Fusing, Nano Lett. 12 (2012) 1873-1878.

[38] H. Sun, Z. Xu, C. Gao, Multifunctional, ultra-flyweight, synergistically assembled carbon aerogels, Adv. Mater. 25 (2013) 2554-2560.

[39] Y. Liu, Z. Xu, J. Zhan, P. Li, C. Gao, Superb Electrically Conductive Graphene Fibers via Doping Strategy, Adv. Mater. 28 (2016) 7941-7947.

[40] L. Peng, Z. Xu, Z. Liu, Y. Guo, P. Li, C. Gao, Ultrahigh thermal conductive yet superflexible graphene films, Adv. Mater. 29 (2017) 1700589.

[41] S. Plimpton, Fast parallel algorithms for short-range molecular dynamics, J. Comput. Phys. 117 (1995) 1-19.

[42] S.J. Stuart, A.B. Tutein, J.A. Harrison, A reactive potential for hydrocarbons with

intermolecular interactions, J. Chem. Phys. 112 (2000) 6472-6486.

[43] T. Ng, J. Yeo, Z. Liu, A molecular dynamics study of the thermal conductivity of graphene nanoribbons containing dispersed Stone–Thrower–Wales defects, Carbon 50 (2012) 4887-4893.

[44] J. Wu, Y. Wei, Grain misorientation and grain-boundary rotation dependent mechanical properties in polycrystalline graphene, J. Mech. Phys. Solids 61 (2013) 1421-1432.

[45] A. Wei, Y. Li, Y. Li, H. Ye, Thermal characteristics of graphene nanosheet with graphane domains of varying morphologies, Comp. Mater. Sci. 138 (2017) 192-198.

[46] Z. Basinski, M. Duesbery, R. Taylor, Influence of shear stress on screw dislocations in a model sodium lattice, Can. J. Phys. 49 (1971) 2160-2180.

[47] N. Chandra, S. Namilae, C. Shet, Local elastic properties of carbon nanotubes in the presence of Stone-Wales defects, Phys. Rev. B 69 (2004) 094101.

[48] Y. Huang, J. Wu, K. Hwang, Thickness of graphene and single-wall carbon nanotubes, Phys. Rev. B 74 (2006) 245413.

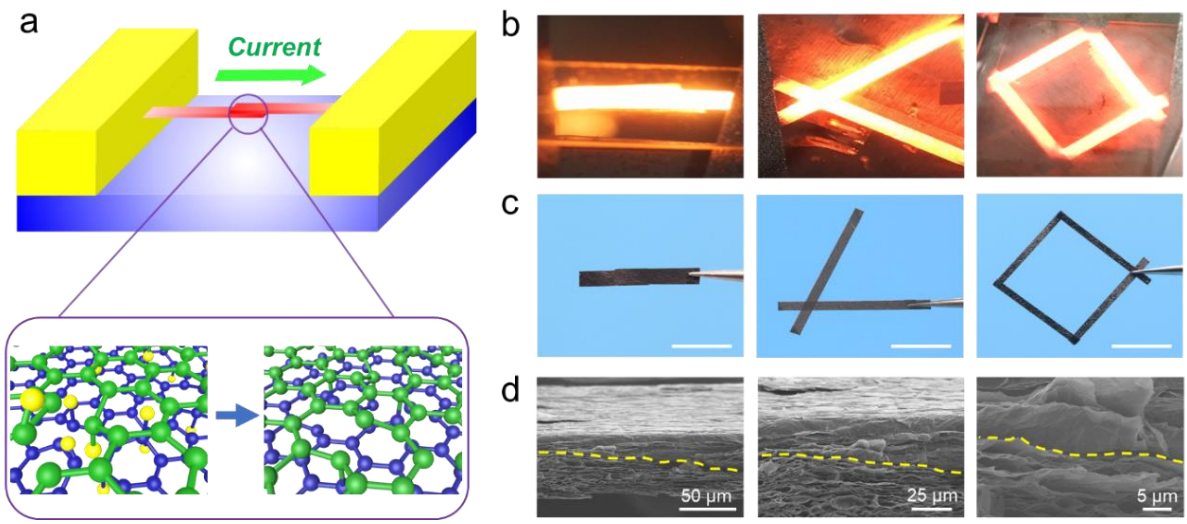

Figure 1. a) Schematic of the welding process of GF-HI. b, c) Photos of the Joule heated GF-HI (b) during the welding process and corresponding welded samples (c). d) Cross-sectional SEM images of the welded GF-HI with an excellent contact, denoted by the yellow dash lines.

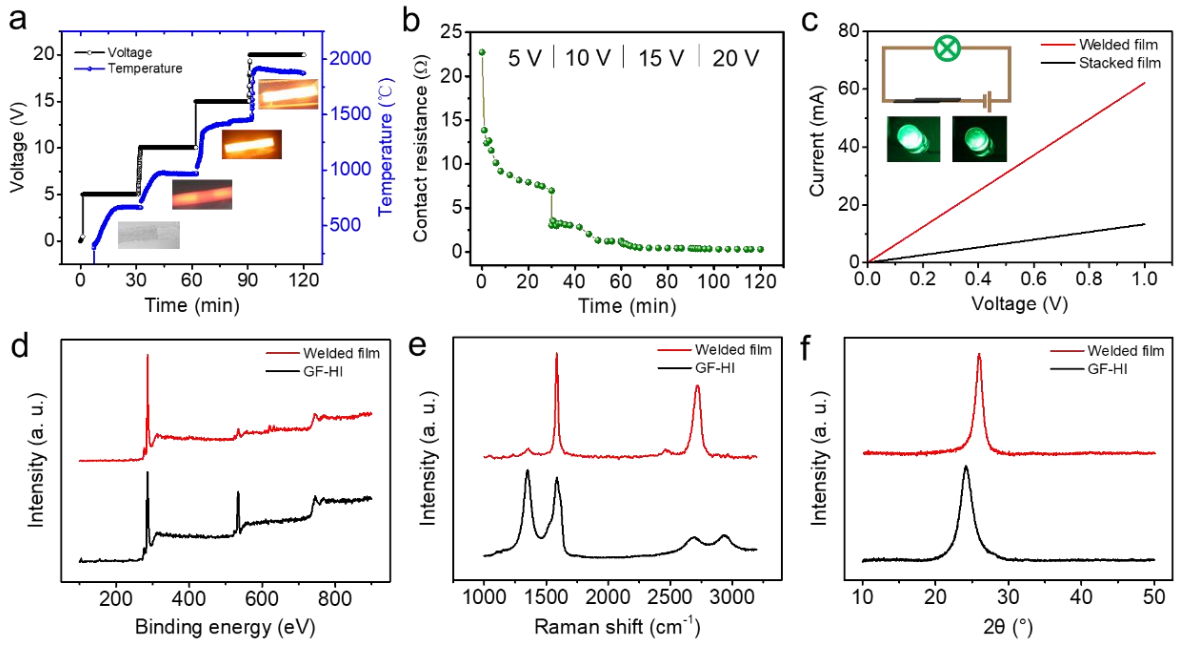

Figure 2. a) Relationship between the temperature of GF-HI and the applied stepwise voltage. Insets are the optical images of the films during the heating process. b) The change of contact resistance during the Joule heating process. c) *I-V* measurement results of the welded films and the mechanically stacked films. Inset: An electric circuit connected by graphene films. The LED lamp connected by the welded films (the lower left) shows higher brightness than that connected by the mechanically stacked films (the lower right). d-f) XPS survey spectra (d), Raman spectra (e), and XRD patterns (f) of the welded films and initial GF-HI.

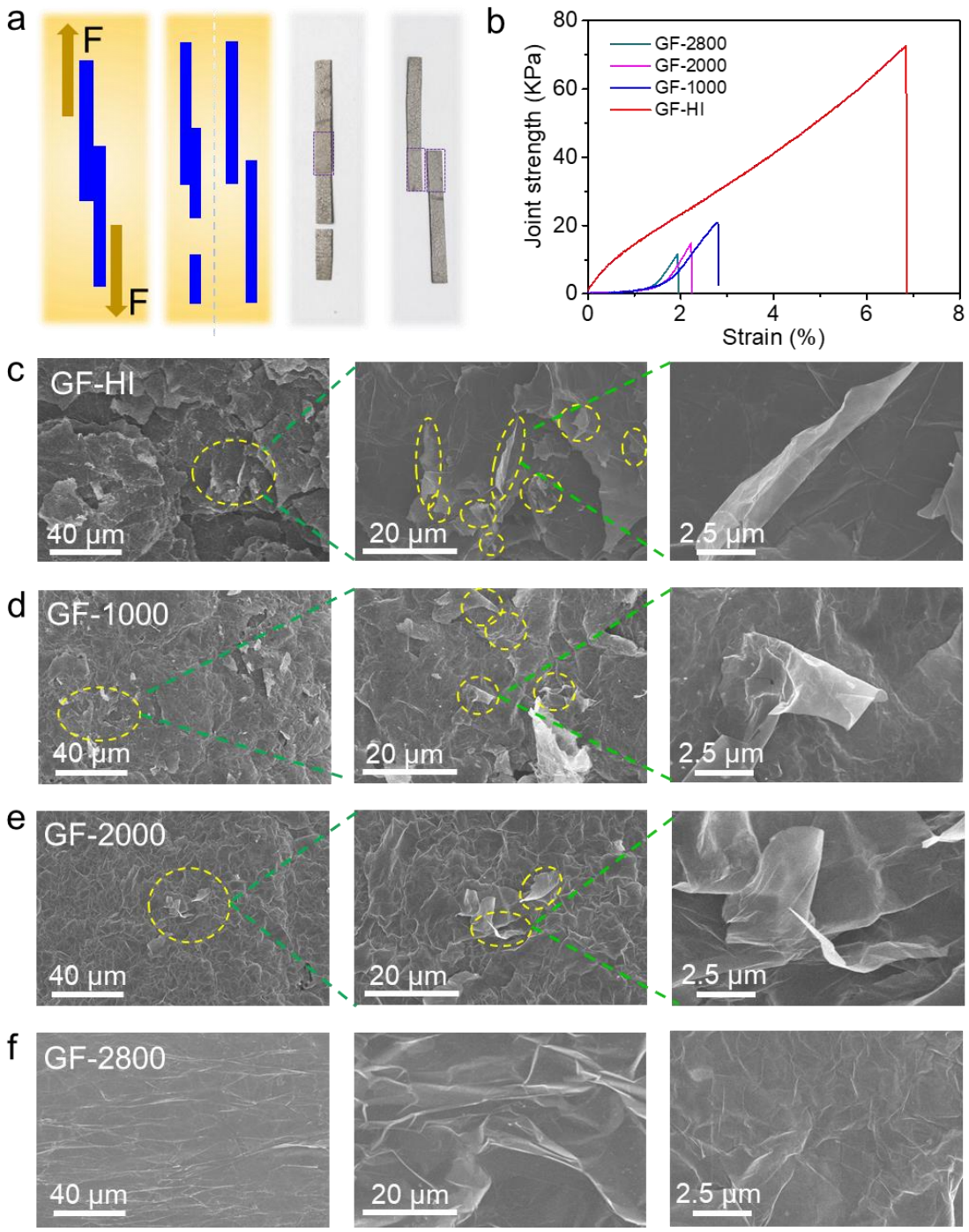

Figure 3. a) Lap shear measurement showing initial state and typical breakage behavior of welded films before and after the lap shear testing. b) Shear stress-strain curves of the Joule heated films preannealed at different temperatures. c-f) SEM images of the failure interfaces of the welded GF-HI (c), GF-1000 (d), GF-2000 (e), and GF-2800 (f). The yellow circles in c-e denote the fragments peeled off the films.

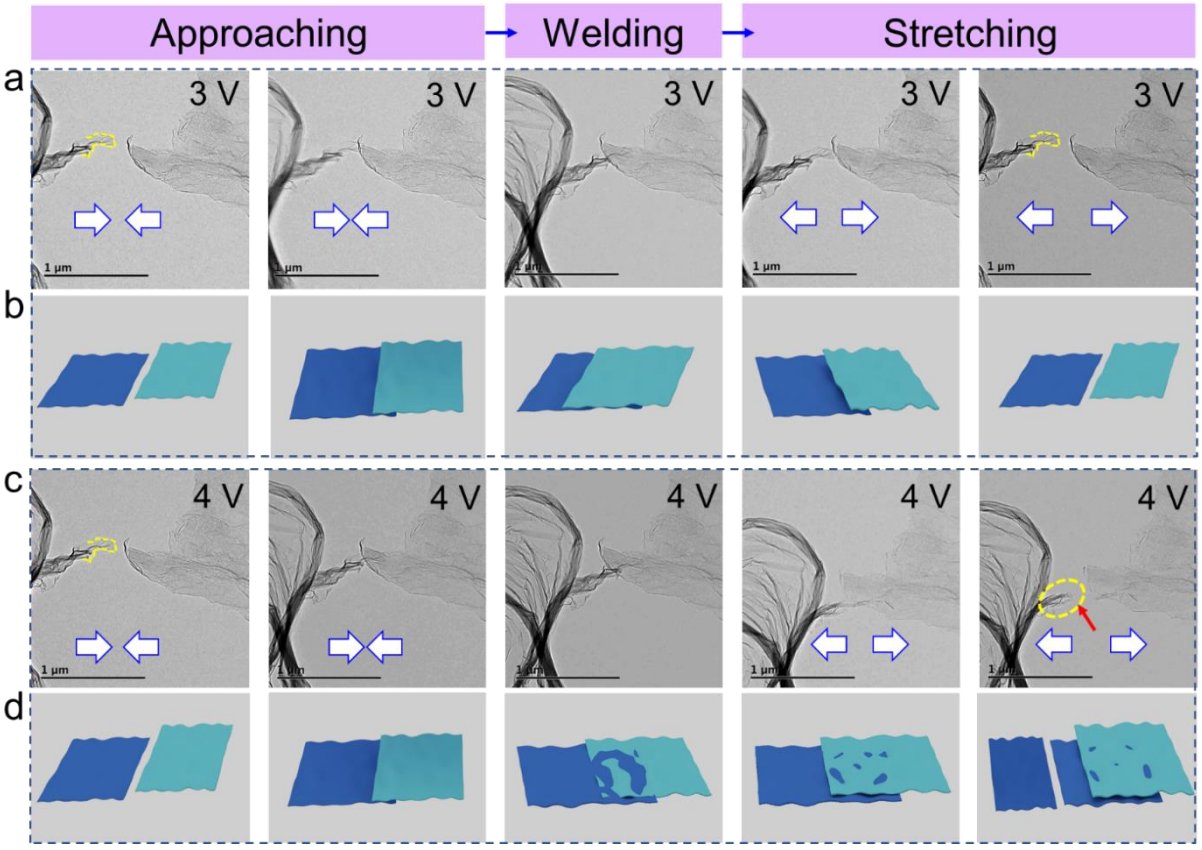

Figure 4. *In-situ* TEM measurements showing electrical Joule connection of graphene sheets at the micro-scale level. Sequential TEM images of rGO sheets and corresponding schematic illustrations during the continuous "approaching-welding-stretching" process at a welding voltage of 3 V (a, b) and 4 V (c, d), respectively. Yellow dashes in a and c indicate the morphology changes of rGO fronts before and after the stretching process.

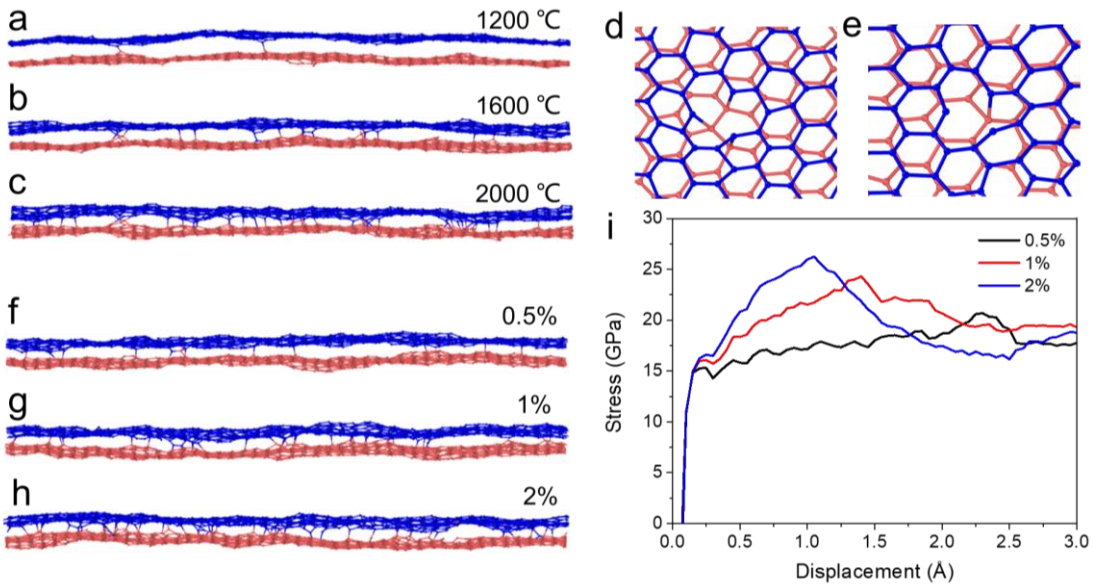

Figure 5. Molecular dynamics simulation results illustrating the formation of covalent bonds between defective bilayer graphene at 1200 °C (a), 1600 °C (b) and 2000 °C (c). d, e) Interlayer covalent bonds forming at the defect sites of the neighboring graphene layers. f-h) Effect of defect densities of the bilayer graphene on the welded structure. i) Stress-displacement curves of welded bilayer graphene with different defect densities.

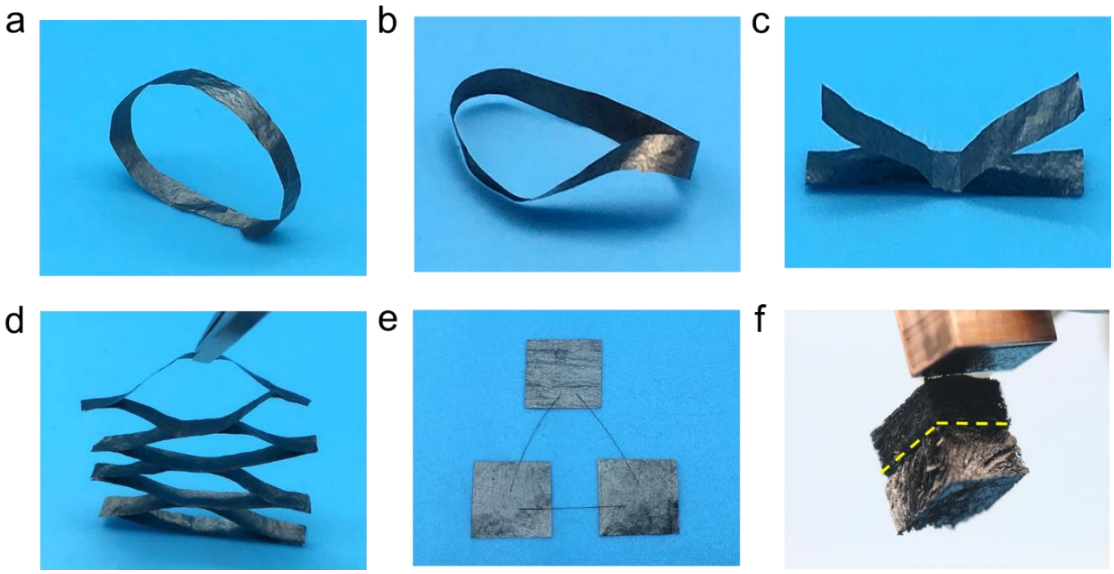

Figure 6. Graphene ring (a) and Möbius band (b) prepared by welding the two ends of a GF-HI. c) "K" shaped structure with a welding point at the center of two individual graphene strips. d) A stretchable kirigami architecture. e) A prototype of all-carbon electronics made by welding graphene films and graphene fibers. f) The welded graphene foams with size of 2.0 cm × 2.0 cm × 1.0 cm.

TOC

Electrical Joule heating is developed as an efficient welding approach to realize robust coalescence of individual graphene assemblies. Such facile high temperature welding strategy will facilitate the bottom-up manufacture of sophisticated carbon-based materials from all-solid-state carbonaceous constituents.